ISSN (Print) 1226-1750
ISSN (Online) 2233-6656
Journal of Magnetics 19(4), 404-410 (2014) http://dx.doi.org/10.4283/JMAG.2014.19.4.404

Design and Analysis of Interior Permanent Magnet Synchronous Motor Considering Saturated Rotor Bridge using Equivalent Magnetic Circuit

Kyung-Hun Shin[1], Ju-Seong Yu[2], Jang-Young Choi[1], and Han-Wook Cho[3]*

[1]Department of Electrical Engineering, Chungnam National University, Daejeon 305-764, Korea
[2]Electric Power Engineering Team, Hyundai Mobis Co., Ltd., Yongin-si 446-912, Korea
[3]Department of Electric, Electronic & Communication Eng. Edu., Chungnam National University, Daejeon 305-764, Korea

(Received 22 October 2014, Received in final form 15 December 2014, Accepted 19 December 2014)

This paper considers the design and performance evaluation of interior permanent magnet synchronous motors (IPMSMs). The initial design such as the sizing and shape design of the stator and rotor is performed for a given load condition. In particular, the equivalent magnetic circuit (EMC) is employed both to design the mechanical parameters of the rotor while considering nonlinear magnetic saturation effect and to analyze the magnetic characteristics of the air-gap of the motor. The designed motor is manufactured and tested to confirm the validity of the design processes and simulated results.

Keywords : interior permanent magnet synchronous motor, initial design, equivalent magnetic circuit, nonlinear saturation effect

1. Introduction

Recently, public concern regarding environmental issues such as global climate change has grown and various alternative technologies have been considered. In particular, hybrid electric vehicle (HEV) technologies, which contribute to reducing global warming, have attracted increased attention, and HEV market penetration has increased rapidly. To further advance of HEV prevalence, electric traction motors with advantageous properties, such as small size, high power density, and high efficiency, are necessary [1]. One suitable motor type is the permanent magnet (PM) machine. Among PM types, IPMSMs are being studied as a promising candidate for many high-power industrial applications operating ranges [2, 3]. IPMSMs produce an additional torque, reluctance torque, by the difference in inductance in the d-q axis as well as the magnetic torque by PMs. Moreover, it has an advantage in high-speed operation in two respects. First, mechanically, they are more solid because of the rotor structure with the inserted PM; thus, there are no circumstances that cause scattering of the PMs at high speed. Second, because there is no additional magnetic air-gap by the sleeve to prevent PM scattering, the mechanical and magnetic air-gap lengths are electrically the same. Thus, the air-gap of IPM-type motors is smaller than in other types and can obtain a larger speed range via flux weakening control (FWC). In this study, a novel design for an IPMSM is introduced and evaluated based on power and torque. In particular, the aim of this study is to improve the initial design process using accurate magnetic loading based on EMC that considers the magnetic saturation of the rotor bridge. The designed model was analyzed in terms of its main characteristics and compared with FEM. In addition, the simulated results are verified by experiment with a manufactured machine.

2. Design and Analysis of IPMSMs using Equivalent Magnetic Circuit

2.1. Design Procedure

Figure 1 shows the block diagram of the design process for the motor. The design process is primarily composed of three steps, which are described in detail below. The first step in the design of the motor is the choice of suitable load conditions for a given application.

Figure 2 shows the characteristic curves of the IPMSMs. The maximum input voltage that the inverter can supply

*Corresponding author: Tel: +82-42-821-8581
Fax: +82-42-821-8886, e-mail: hwcho@cnu.ac.kr

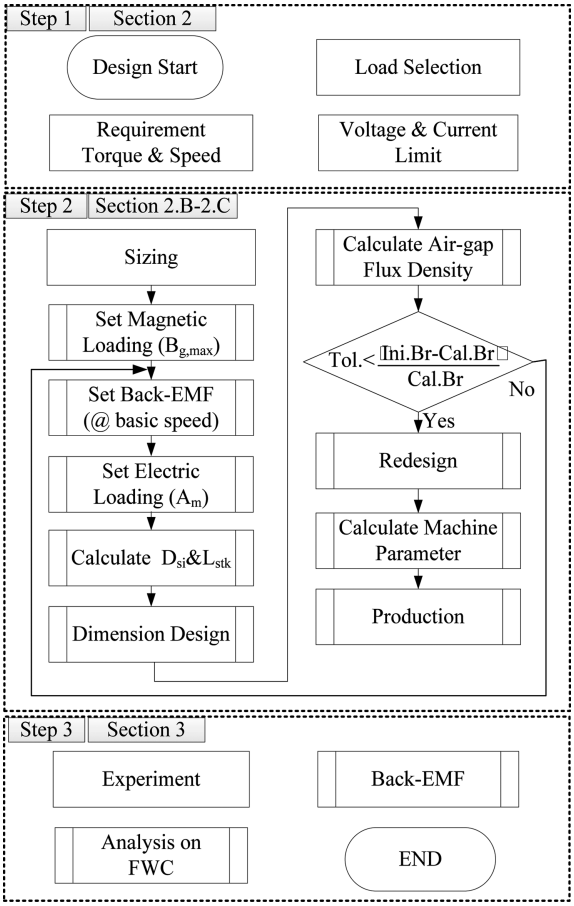

Fig. 1. Design process of the motor.

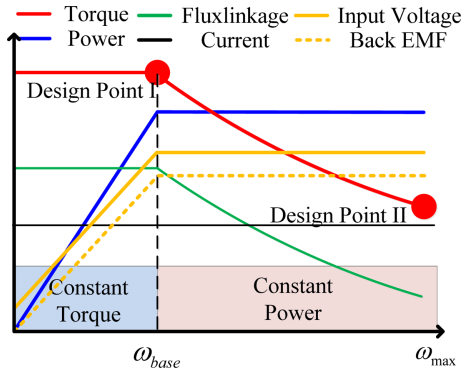

Fig. 2. (Color online) Characteristic curve of IPMSMs.

to the machine is limited by the DC link voltage and the PWM strategy used. Additionally, the base speed is limited by the maximum voltage and the electro-magnetic characteristics of the machine. Table 1 presents the required characteristics, namely, base speed, rated power, and maximum voltage. The second step in the design of the motor is determining the size of the motor. The sizing is used to select the proper volume for the motor for the given requirements. Before sizing, the basic values of the

Table 1. Required characteristics of IPMSMs.

Specification	Value	Unit
Base speed	3200	rpm
Power at rated	400	W
Maximum Voltage	12	V

design (such as the air-gap, slot opening, current density, and wire size) are determined from experience and applications. Using the loading distribution method and the basic design values, the magnetic and electric loading influencing the output of the motor can be separated. Finally, the third step in the design of the motor is an experimental test in the no-load and load conditions. Because the back-EMF increases with increasing motor speed, FWC (an operating method) is used to obtain the voltage margin and help the machine to operate at higher speeds. By reducing the magnetic flux of the PM, the back-EMF is controlled and the voltage margin can be kept in the high speed, constant power region, as shown in Fig. 2.

2.2. Sizing

The equation for specific magnetic loading is expressed as

$$B_{g,\max} = \frac{\phi_f}{\alpha_p \tau_p L_{stk}} \tag{1}$$

where α_p is the effective pole arc coefficient, ϕ_f is the linkage flux of the air-gap, τ_p is the pole pitch, and L_{stk} is the stack length of the motor.

The equation for the specific electric loading is expressed as

$$A_m = \frac{2m\sqrt{2}N_{ph}I_{a,rms}}{\pi D_{si}} \tag{2}$$

$$Z = 2mN_{ph} \tag{3}$$

where I_a is the phase current, Z is the number of the conductor, m is the number of the phase, N_{ph} is the number of turns, and D_{si} is the inner diameter of the rotor.

Therefore, Z for the three-phase motor is

$$Z = 6N_{ph} \tag{4}$$

The equation for output power from the loading distribution method is expressed as

$$P_{out} = (0.5\pi^2 k_w n_{rps} B_{g,\max}) D_{si}^2 L_{sik} \tag{5}$$

where n_{rps} is the synchronous speed and k_w is the coefficient of winding. The electromagnetic torque

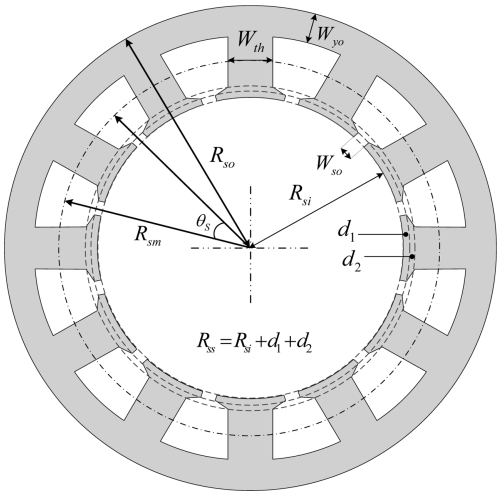

Fig. 3. Basic stator structure and parameter definition.

$$T_{out}=\left(\frac{\pi}{4}k_w B_{g,\max}A_m\right)D_{si}^2 L_{sik} \tag{6}$$

The equation for the size can be rewritten as

$$D_{si}^2 L_{sik}=\frac{T_{out}}{C_o} \tag{7}$$

where C_o is the coefficient of power.

From Eq. (7), the size of the motor can be roughly determined using the power coefficient method.

After obtaining the approximate size of the motor, the detailed design is carried out considering design parameters such as the width and height of the teeth, the width of the yoke, and the slot area.

Figure 3 shows the stator structure and parameter definition used to design the detailed shape of the machine. In this figure, R_{si} is the inner radius of the stator, R_{sm} is the radius of the teeth in the middle, R_{so} is the outer radius of the stator, θ_s is the slot pitch, and d_1+d_2 is the shoe height. The width of the slot opening (W_{so}) is expected to be approximately two or three times the wire sizes.

The relation between the magnetic flux in the air-gap and the shape of the stator core is expressed as

$$\phi_f=\frac{QB_{tm}W_{th}L_{stk}}{2p} \tag{8}$$

where Q is the number of the slot and B_{tm} is the saturated magnetic flux density of the teeth.

The equation for the width of the teeth of the stator core can be rewritten as

$$W_{th}=\frac{2p\phi_f}{QB_{tm}L_{stk}} \tag{9}$$

Additionally, approximately 10% to 20% of the width of the teeth is pretty easy for the height of the shoes

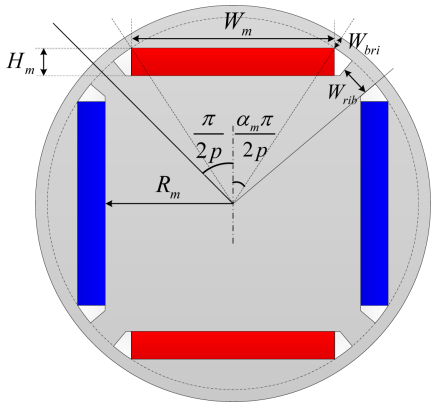

Fig. 4. (Color online) Rotor structure of IPM type.

(d_1+d_2). In the same context, the width of the yoke is expressed as

$$W_{yo}=\frac{\phi_f}{2B_{ym}L_{stk}} \tag{10}$$

where B_{ym} is the saturated magnetic flux density of the yoke.

The relation between the slot area and the radius of the teeth in the middle can be expressed as

$$A_s=2\alpha_{slot}R_{sm}\theta_s(R_{sm}-R_{ss}) \tag{11}$$

where a_{slot} is the ratio of the slot pitch to the width of the teeth.

The initial design of the stator is complete after calculating the above design parameters for a motor. Figure 4 shows the rotor structure of an IPM-type machine. The parameters below should be determined in the design of the rotor shape of bar-type IPMSMs [4].

$$W_m=2\left(\frac{D_{ro}}{2}-W_{bri}\right)\sin\left(\alpha_m\frac{\pi}{2p}\right) \tag{12}$$

$$R_m=\left(\frac{D_{ro}}{2}-W_{bri}\right)\cos\left(\alpha_m\frac{\pi}{2p}\right)-H_m \tag{13}$$

$$W_{rib}=\frac{\pi}{p}(1-\alpha_m)\sqrt{\left(\frac{W_m}{2}\right)^2+(R_m)^2} \tag{14}$$

$$\alpha_m=\frac{2p}{\pi}\arctan\left(\frac{W_m}{2R_m}\right) \tag{15}$$

where D_{ro} is the diameter of the rotor, W_m is the PM width, R_m is the radius of the magnet's bottom position, W_{bri} is the bridge width, W_{rib} is the rib width, and α_m is the pole-arc ratio.

2.3. Equivalent Magnetic Circuit Modeling while considering Saturated Rotor Bridge

Because the rotor's inner structure is complex, it is

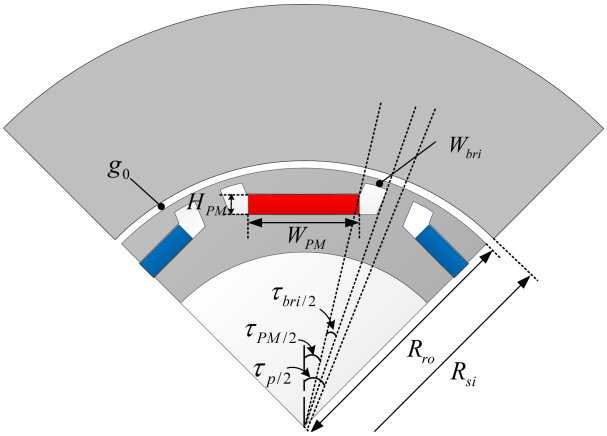

Fig. 5. (Color online) Analysis model for a lumped equivalent magnetic circuit.

difficult to predict the magnetic field distribution based only on the motor geometry and dimensions. The extensively used lumped equivalent magnetic circuit (EMC) method is adopted to highlight the influence of rotor design parameters and provide a simple and useful means of evaluation at the early stages of design [5]. The IPMSM rotor structure uses the conventional single-layer design. To analyze the magnetic characteristics of the motor using the lumped EMC, several assumptions are required [6, 7]:

1. The permeability of iron is infinite.

(except in the highly saturated bridge region between the flux barriers and the rotor's surface).

2. The magnetic saturation effect is ignored.

(except in the bridge regions, which are given by a constant saturation flux density $B_{sat.}$ or input B-H data).

3. The effect of irreversible demagnetization of the PMs is not considered.

A slotless IPMSM with 8 poles is shown in Fig. 5.

Table 2. Specifications and initial design parameters for EMC.

Item	Symbol	Value	Unit
Pole Number	p	8	-
PM remanent flux	B_r	1.3	T
Height of PM	H_{PM}	2.8	mm
Width of PM	W_{PM}	15.5	mm
Inner radius of stator	R_{si}	36	mm
Length of air-gap	g_0	0.5	mm
Thickness of bridge	W_{bri}	0.5	mm
Length of axial stack	L_{stk}	18	mm
Outer radius of rotor	R_{ro}	35.5	mm
Pole-arc	$\tau_p(2\,\tau_{p/2})$	27.13	Deg.
Magnet-arc	$\tau_{PM}(2\,\tau_{PM/2})$	25.036	Deg.
Bridge-arc	$\tau_{bri}(2\,\tau_{bri/2})$	5.12	Deg.

Table 2 lists the initial parameters of this model. Because the fundamental component of the magnetic flux density in the air gap is of interest, in this paper, we did not consider the slotting effect.

Figure 6 shows a lumped magnetic circuit associated with the flux produced by the single-layer PM segment. To perform the above-presented lumped EMC, the following equations are solved in sequence [8]. The flux from the PMs to the bridge region can be calculated as follows

$$\phi_r = B_r \cdot A_{PM} = B_r \cdot W_{PM} \cdot L_{stk} \tag{16}$$

$$\phi_{bri} = B_{sat} \cdot A_{bri} = B_{sat} \cdot W_{bri} \cdot L_{stk} \tag{17}$$

$$\frac{\phi_g}{2} = \frac{\phi_r}{2} - \left(\frac{\phi_{PM}}{2} + \frac{\phi_{FB}}{2} + \phi_{rib}\right) \tag{18}$$

where A_{PM} and A_{bri} are the area of the PM and bridge, respectively. ϕ_g, ϕ_{bri}, ϕ_{FB}, and ϕ_{rib} are the magnetic flux of the air-gap, bridge, flux-barrier, and rib, respectively. $B_{sat.}$ is the saturated magnetic flux density in the bridge region.

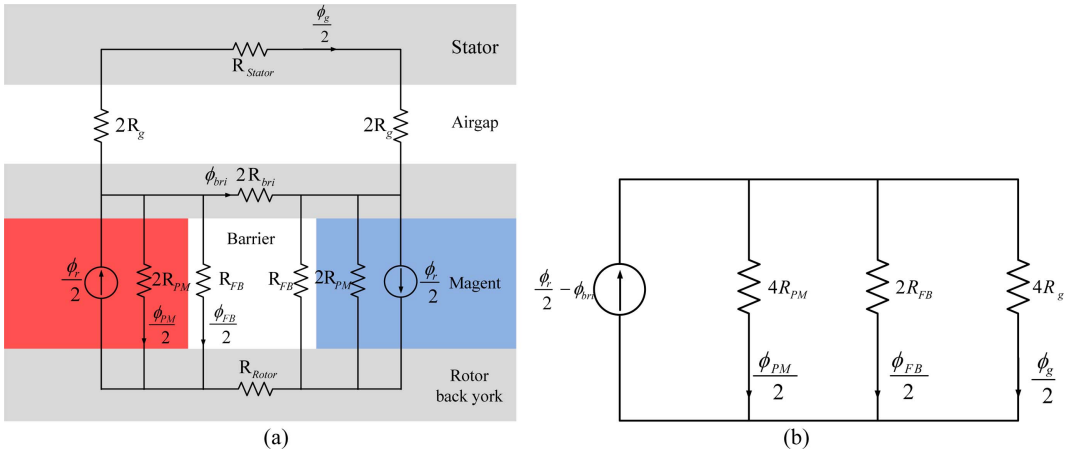

Fig. 6. (Color online) Lumped magnetic circuit.

The reluctances in each region are expressed as follows

$$R_g = \frac{g_o}{\mu_o \cdot A_g} \tag{19}$$

$$R_{PM} = \frac{H_{PM}}{\mu_o \cdot \mu_r \cdot A_{PM}} = \frac{H_{PM}}{\mu_o \cdot \mu_r \cdot W_{PM} \cdot L_{stk}} \tag{20}$$

$$R_{FB} = \frac{H_{FB\_ave}}{\mu_o \cdot W_{FB\_ave} \cdot L_{stk}} \tag{21}$$

where R_g (R_{PM}, R_g) is the reluctance of the air-gap (PM, barrier) and H_{FB_avg} (W_{FB_avg}) is the height (width) of the barrier. g_o and μ_o are the air-gap length and the space permeability, respectively.

To obtain the flux density in the air-gap, the area of the middle of the air-gap is calculated as follows

$$A_g = \alpha_p \frac{2\pi(R_{si} - g_o/2)}{2p} L_{sik} \tag{22}$$

Figure 7 shows the air-gap flux density distribution for the slotless model and compares it with those of EMC and FEM. In the above analytical model, the air-gap flux distribution in the bridge region causes significant difference in the flux density waveform (under several assumptions). If the bridge-arc of the flux barrier is too wide to be ignored, the predicted air-gap flux density waveform will produce an obvious error, as shown Fig. 7. As an expansion of the presented lumped EMC method, an improved analysis considering the saturation of the bridge region is proposed; this method exactly predicts the flux density waveform in the bridge region. The bridge region is composed of integral circuit units of air-gap reluctance ΔR_{go} and bridge reluctance ΔR_{bri}, as shown Fig. 8.

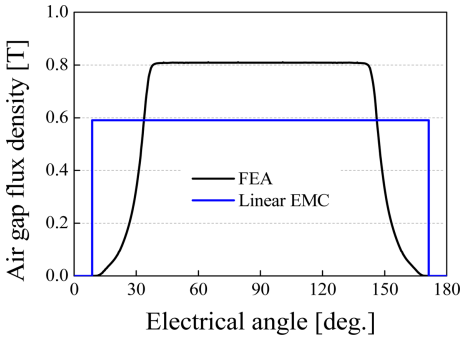

Fig. 7. (Color online) Air-gap flux density distribution with slotless model.

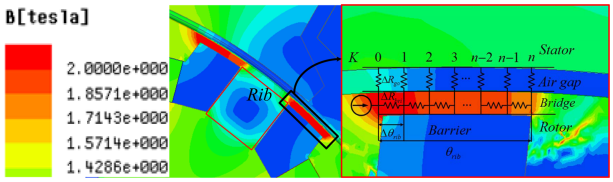

Fig. 8. (Color online) Equivalent circuit of segmented bridge region.

The segmented reluctances of the bridge region in Fig. 8 are expressed as follows

$$\Delta R_{go} = \frac{g_o}{\mu_o \cdot (R_{si} \cdot \Delta\theta \cdot \pi/180) \cdot L_{sik}} \tag{23}$$

$$\Delta R_{rib} = \frac{(R_{ro} \cdot \Delta\theta_{bri} \cdot \pi/180)}{\mu_o \cdot \mu_r \cdot W_{bri} \cdot L_{stk}} \tag{24}$$

where R_{ro} and μ_r are the outer radius of the rotor and the relative permeability, respectively.

As the bridge region is divided into a larger number of reluctances, the more closely the results of the analysis are agreement. The predicted air-gap flux density shows good agreement with FEM, as shown in Fig. 9. Figure 9 (a) shows the air-gap flux density with only one bridge

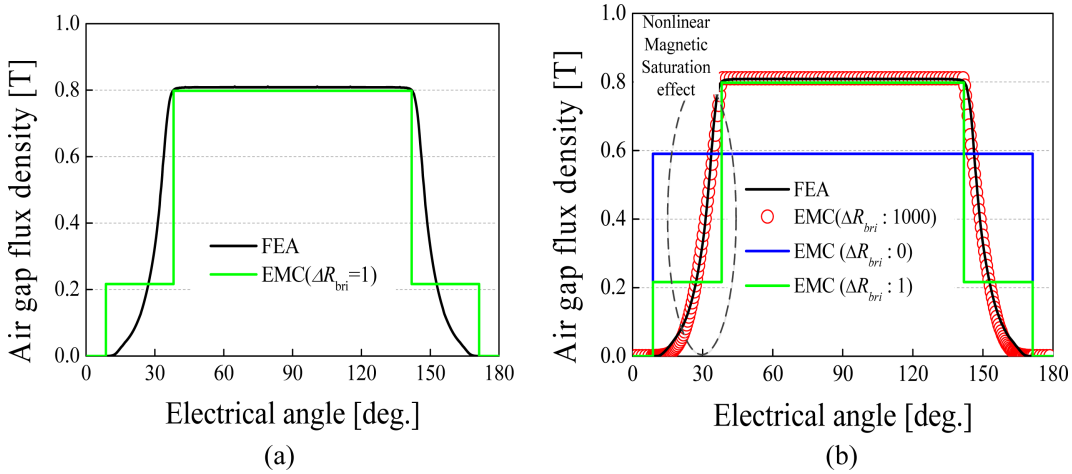

Fig. 9. (Color online) Air-gap flux density considering ΔR_{bri}. (a) number of ΔR_{bri}: 1 and (b) number of ΔR_{bri}: 1000.

Table 3. Design parameters of manufactured machine.

Item	Value	Item	Value
Stator Outer/Inner Diameter	116/72 mm	Rotor Outer/Inner Diameter	71/48 mm
Bridge Thickness	0.5 mm	Air-gap	0.5 mm
Rib	4 mm	Remanent Fluxdensity	1.3 T
Number of Slot	12	Number of Pole	8
Core Material	50PN470	Magnet Material	N42SH
Winding	concentrated	Axial Length	18 mm

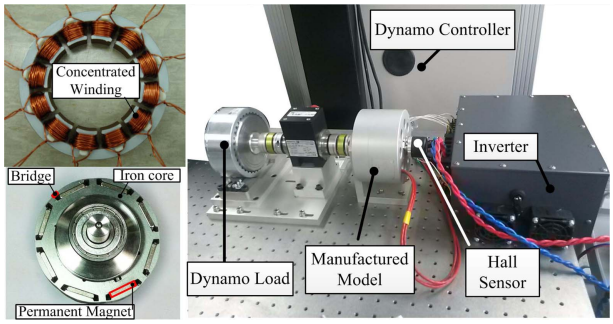

Fig. 10. (Color online) Manufactured IPMSM and test equipment for experiment.

reluctance. Figure 9(b) shows the air-gap flux density with divided bridge reluctances.

3. Experimental Results and Discussion

A previous paper proposed optimum designs of the stator and rotor shape for IPMSMs using RSM [9]. As a result, we can significantly reduce the cogging torque (which causes vibration and noise) by selecting the optimal design point. Additionally, the results include a feature that slightly decreased other performances.

The detailed specifications of the initial IPMSM are shown in Table 3. Figure 10 shows the manufactured IPMSM and the test equipment used in the experiment. The back-EMF induced in a stator winding due to magnet flux crossing the air-gap is given by the rate of change in flux linkage with respect to time [10].

Figure 11 shows a comparison of a prediction with nonlinear FEM and an experimental measurement for the phase of the back-EMF of the manufactured machine. Figure 11 shows that the predicted results agree well with measurements in terms of both waveform and amplitude. Figure 12 shows the torque versus speed curve. The

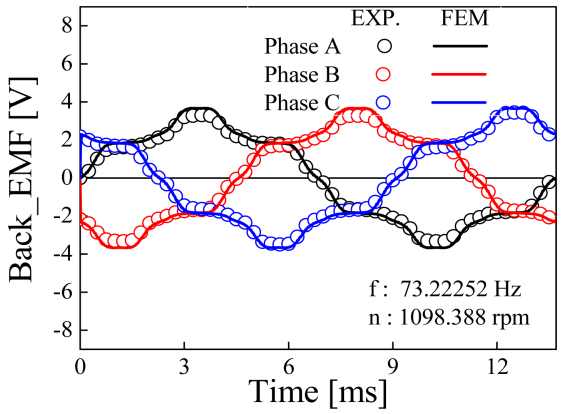

Fig. 11. (Color online) Three phase back-EMF of measured initial model.

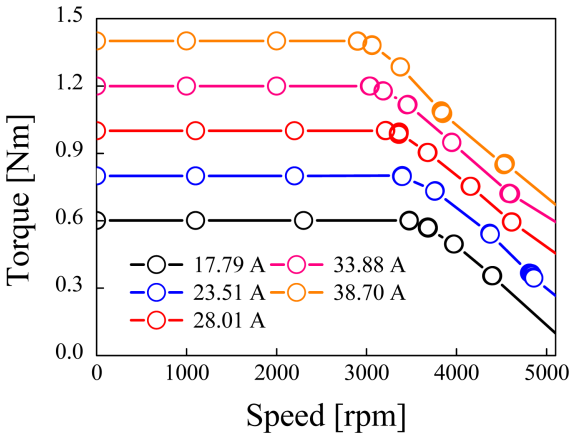

Fig. 12. (Color online) Torque-speed performances according to phase current.

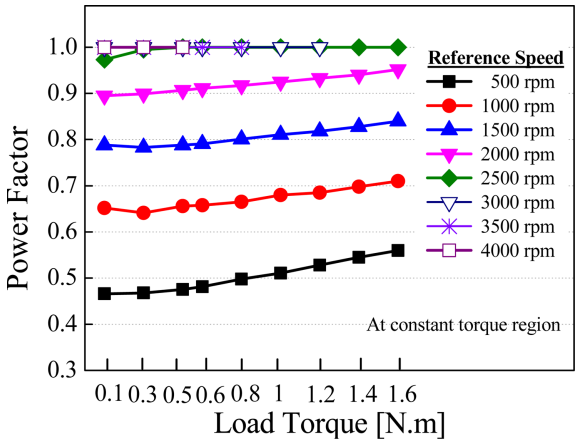

Fig. 13. (Color online) Power factor versus reference speed in constant torque region.

results show the characteristic performance of the model for the load condition. These results are obtained for a variety of load-conditions from 18 [A] to 40 [A].

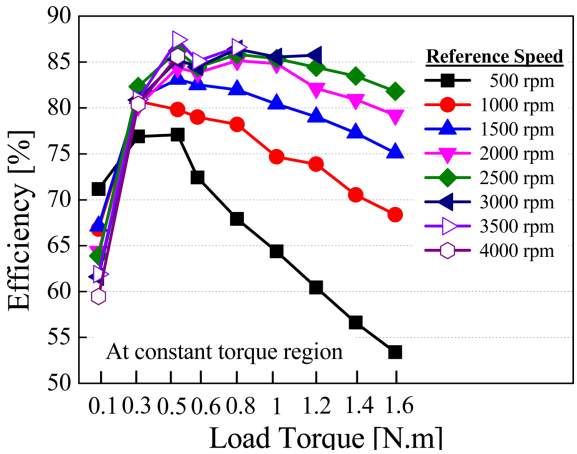

Fig. 14. (Color online) Efficiency versus reference speed in constant torque region.

Figure 13 shows the power factor characteristics for different reference speeds under speed control and the load torque in the constant torque region. At 2500 rpm and above, the power factor remains near 1, regardless of the load torque, as shown in Fig. 13. Figure 14 shows the efficiency of the motor for different reference speeds and load torques. High efficiency is shown above 2000 rpm. The load torque was from 0.5 [N·m] to 1.6 [N·m].

4. Conclusion

In this study, detailed initial design criteria for IPMSMs were determined. First, the load condition is selected in accordance with the application. Second, the magnetic and electric loading (which influence the output of the motor) are separated. Initial design is performed using the loading distribution method. Magnetic loading is defined by EMC while considering the nonlinear magnetic saturation effects of the rotor bridge. Finally, the performance of the designed motor was verified using FEM and experiments.

Acknowledgement

This work was supported by the National Research Foundation (NRF) grant funded by the Korea goverment (MSIP) (No. 2013R1A2A2A04007384).

References

[1] Tatsuro Arakawa, Masatsugu Takemoto, Satoshi Ogasawara, Koji Inoue, Osamu Ozaki, Hirfumi Hojo, and Hiroyuki Mitani, IEEE Transn. Magn. **47**, 3602 (2011).
[2] E. C. Lovelace, T. M. Jahns, and J. H. Lang, IEEE Trans. Ind. Appl. **36**, 723 (2000).
[3] Y. Abdel-Rady, I. Mohamed, and T. K. Lee, IEEE Trans. Energy Convers. **21**, 636 (2006).
[4] Jae-Nam Bae, Ph.D. Thesis, Hanyang University, Korea, (2010).
[5] Liang Fang, Ph.D. Thesis, Hanyang University, Korea (2011).
[6] Nady Boules, IEEE Trans. Ind. Appl. **1A-21**, 4 (1985).
[7] C. Mi, M. Filippa, W. Liu, and R. Q. Ma, IEEE Trans. Magn. **40**, 1 (2004).
[8] Nicole Bianchi and Thomas M. Jahns, Tutorial Course Notes; Seattle, Oct. (2004).
[9] Ju-Seong Yu, Han-Wook Cho, Jang-Young Choi, Seok-Myeong Jang, and Sung-Ho Lee, J. Power Electron. **13**, 546 (2013).
[10] D. C. Hanselman, "Brushless Permanent Magnet Motor Design", The Writer's Collective (2003).